The Power Spectra of Polarized, Dusty Filaments

KEVIN M. HUFFENBERGER, ADITYA ROTTI, AND DAVID C. COLLINS

¹Department of Physics, Florida State University, Tallahassee, Florida 32306, USA ²Jodrell Bank Centre for Astrophysics, School of Physics and Astronomy, The University of Manchester, Manchester M13 9PL, UK

ABSTRACT

We develop an analytic model for the power spectra of polarized filamentary structures as a way to study the Galactic polarization foreground to the Cosmic Microwave Background. Our approach is akin to the cosmological halo-model framework, and reproduces the main features of the Planck 353 GHz power spectra. We model the foreground as randomly-oriented, three-dimensional, spheroidal filaments, accounting for their projection onto the sky. The main tunable parameters are the distribution of filament sizes, the filament physical aspect ratio, and the dispersion of the filament axis around the local magnetic field direction. The abundance and properties of filaments as a function of size determine the slopes of the foreground power spectra, as we show via scaling arguments. The filament aspect ratio determines the ratio of B-mode power to E-mode power, and specifically reproduces the Planck-observed dust ratio of one-half when the short axis is roughly one-fourth the length of the long axis. Filament misalignment to the local magnetic field determines the TE cross-correlation, and to reproduce Planck measurements, we need a (three-dimensional) misalignment angle with a root mean squared dispersion of about 50 degrees. These parameters are not sensitive to the particular filament density profile. By artificially skewing the distribution of the misalignment angle, this model can reproduce the Planck-observed (and parity-violating) TB correlation. The skewing of the misalignment angle necessary to explain TB will cause a yet-unobserved, positive EB dust correlation, a possible target for future experiments.

Keywords: Cosmic microwave background radiation, Interstellar medium

1. INTRODUCTION

Polarized Galactic microwave emission poses a challenge to the search for primordial *B*-mode polarization in the Cosmic Microwave Background (CMB). The *B*-mode signal could provide direct constraints on the energy scale of inflation, but the Milky Way foregrounds may outshine it at all frequencies, everywhere on the sky (Planck Collaboration et al. 2016a; Abazajian et al. 2016; Hervías-Caimapo et al. 2016; Thorne et al. 2017; Remazeilles et al. 2018; Hanany et al. 2019). We have a limited understanding of this foreground, and we must learn more to ensure the reliability of future *B*-mode measurements.

The foreground emission involves the turbulent interplay of gas, dust, and magnetic fields in the Galaxy's interstellar medium (ISM). The magnetic fields organize the flow and control the orientation of grains that give rise to the polarized dust signal. Although Planck's 353 GHz polarization channel has given us a first look, several features of the dust polarization remain without physical explanations.

For example, the amplitude of dust polarization B-mode power is approximately half of E-mode power, $A_{BB}/A_{EE}=0.53\pm0.01$, when fit on a large portion of the sky (for $f_{\rm sky}^{\rm eff}=0.52$ –0.71). Smaller patches also show the same mean value $A_{BB}/A_{EE}=0.51$, with small patch-to-patch dispersion $\sigma_{BB/EE}=0.18$ (Planck Collaboration et al. 2016a, 2018). This observation defied pre-Planck expectations. Random polarization orientations, or coherent orientations overlaying random polarization intensity fluctuations, both yield equal amounts of E and B (Zaldarriaga 2001; Kamionkowski & Kovetz 2014).

We have some understanding of dust physics and its relationship to polarization modes. The amplitude and orientation of the dust signal is set by the integrated column density and magnetic field orientation. For E to have more power than B qualitatively means that density fluctuations (structures in the ISM density field) must prefer orientations parallel or perpendicular to the local magnetic field (Rotti & Huffenberger 2019). This picture is borne out by measurements of the magnetic field orientation in individual, bright, filamentary struc-

tures in the Planck 353 GHz data (Planck Collaboration et al. 2016b). This is further validated by the observations that linear structures in neutral hydrogen emission, highlighted by a Rolling Hough Transformation, also correlate with the magnetic field direction indicated by Planck dust polarization (Clark et al. 2014, 2015).

Other aspects of the dust polarization also need physical explanations. Both E-mode and B-mode spectra follow power laws $(C_{\ell} \propto \ell^{\alpha})$, with approximately the same slope, $\alpha_{BB} = -2.42 \pm 0.02$ and $\alpha_{EE} = -2.45 \pm 0.03$. (Planck Collaboration et al. 2016a, 2018) There is a positive correlation between dust intensity and E-mode polarization (noted by Caldwell et al. 2017), with correlation coefficient $r_{TE} = 0.357 \pm 0.003$ (Planck Collaboration et al. 2018) and significant scatter depending on the sky area but little evidence for scale dependence. Perhaps more intriguing is a parity-violating, positive TB correlation (Planck Collaboration et al. 2018). Finally, the amplitude of dust polarization power correlates to intensity in patches, roughly as $\langle I \rangle_{\rm patch}^{1.9}$, for both E and B (Planck Collaboration et al. 2016a).

A few works have already tried to address these observations. Caldwell et al. (2017) examined the dust polarization power spectra of slow, fast, and Alfvén MHD waves in terms of two parameters: the ratio of gas to magnetic pressure, and the anisotropy of the MHD modes around the background field direction. They found two regions of parameter space that can account for the E to B ratio and positive TE correlation but judged that these scenarios are unlikely due to the uniformity of the polarization power spectrum across the sky, and instead suggested that Planck may be seeing large scale displacements that are driving the turbulent ISM, rather than the turbulence itself.

On the other hand, Kandel et al. (2017) argued with a similar analysis that the observed E/B power ratio can be realized in an analytic MHD model, so long as the turbulent flow is sub-Alfvénic. Kandel et al. (2018) extended this analysis to examine the TE correlation and synchrotron emission. Such an MHD analysis assumes that the density is passively advected by the turbulent motions, an assumption that may be violated for the cold phase of the ISM. The formation of filaments in the multiphase ISM (per Xu et al. 2019) could also affect this MHD analysis.

Other works approach the problem using MHD simulations. For the most part, the ISM is filled with trans- and super-sonic flows, which are non-linear (e.g. Elmegreen & Scalo 2004; Burkhart et al. 2010). Both Kritsuk et al. (2018) and Kim et al. (2019) made MHD simulations of the ISM, and modeled the dust polarization signals. Both works find slopes and power ratios

that are reasonably close to the observed values, but the slopes are especially sensitive to the masking procedure. What MHD simulations do not provide is a straightforward and direct way to understand why these polarization properties arise.

Here we seek to gain physical intuition with very simple models of polarized filaments. We do not yet know to what degree filamentary structures contribute to the polarization foreground. There is certainly evidence for filamentary structure in HI and CMB data (Clark et al. 2014; Planck Collaboration et al. 2016b) as well as in simulations of the interstellar medium (de Avillez & Breitschwerdt 2005; Hennebelle 2013). Using the HI morphology alone, Clark & Hensley (2019) were able to reproduce to high correlation the statistics of the polarized sky, which indicates that filaments may be a significant contribution. However, apparent filaments found in HI velocity channel maps may not be coherent density structures (physical filaments). Instead they could be coherent velocity structures without the need for associated density enhancements (Yuen et al. 2019). Considering this second viewpoint, Hu et al. (2020) used a combination of velocity gradients and principal component analysis to predict polarization properties of the ISM, and also reproduced the microwave sky to high correlation.

Filamentary structure is a natural consequence of strongly magnetized turbulence (Goldreich & Sridhar 1995; Kritsuk & Norman 2004; Heiles & Haverkorn 2012; Hennebelle 2013; Micelotta et al. 2018; Ossenkopf-Okada & Stepanov 2019; Xu et al. 2019; Beattie et al. 2019). The distribution of filament properties is a nontrivial function of the state of the gas. The properties of velocity and magnetic field fluctuations in MHD turbulence are better understood (e.g. Brandenburg & Lazarian 2013) than the statistics of density, particularly for turbulence with high sonic Mach number. For sub- and trans-sonic gas, eddies are elongated in the direction of the local mean magnetic field (Goldreich & Sridhar 1995; Xu et al. 2019), while for supersonic gas, shocks form perpendicular to the local mean field (Soler et al. 2013; Beattie et al. 2019). The nearby ISM is certainly a mixture of components (McKee & Ostriker 1977; Vazquez-Semadeni 2009: Heiles & Haverkorn 2012), but typically seems to have low velocity relative to the speed of sound for the majority of the nearby high-latitude gas (Redfield & Linsky 2004; McClure-Griffiths et al. 2006; Kalberla et al. 2016; Skalidis & Pelgrims 2019; Clark & Hensley 2019). Our model depends on the distribution of filament properties and their alignment with the field, and thus will depend on the properties of the kinematics of the gas. The exact details of this relationship is the focus of ongoing research.

The purpose of this paper is to explore what polarization power spectra are possible for filaments, and what the observed power spectra can tell us about their physical properties. We compute their temperature and polarization power spectra using a method akin to the cosmological halo model (e.g. Seljak 2000; Cooray & Sheth 2002). However, instead of spherical halos, we use magnetized, prolate-spheroidal filaments as the basic ingredients, and integrate over their population. Because turbulence is not well-understood in the multiphase ISM, we do not start with many prior constraints on the statistics of the filament parameters.

We organize this paper so that in Section 2 we describe our formalism for characterizing the filament signal and for computing the power spectra. In Section 3, we show the power spectra and discuss how the parameters of the filament population affect them. In Section 4, we conclude and discuss the implications and possible future directions. An appendix describes how the distributions of filament and magnetic field orientations in three dimensions appear when projected onto the plane of the sky.

2. METHOD

We define a projected filament profile, f(x), upon which we paint the temperature (i.e. intensity) and polarization signals. Thus the temperature profile is:

$$T(\boldsymbol{x}) = T_0 f(\boldsymbol{x}),\tag{1}$$

for sky position x. We model the polarization with an overall polarization fraction and polarization direction. In terms of the Stokes parameters, the polarization for a filament is

$$X(\mathbf{x}) = (Q + iU)(\mathbf{x})$$

$$= f_{\text{pol}} \exp(2i\psi_{\text{pol}})T_0 f(\mathbf{x}).$$
(2)

In the HEALPix polarization convention (Górski et al. 2005), the +x-axis points south and the polarization angle $\psi_{\rm pol}$ increases east of south. Because we will integrate over angles in our computation of the power spectrum (and because E and B fields are coordinate independent) we can analyze a filament that has its long axis aligned (in projection) with the x-axis without loss of generality. For simplicity, we assume that the intrinsic, microphysical contribution to $f_{\rm pol}$ is common to all filaments, although we will account for geometrical and projection effects in this work. If the long axis of that filament were aligned with the local magnetic field, the precession of the dust grains would cause the polarization angle to be $\psi_{\rm pol} = 90^{\circ}$, perpendicular to the filament axis.

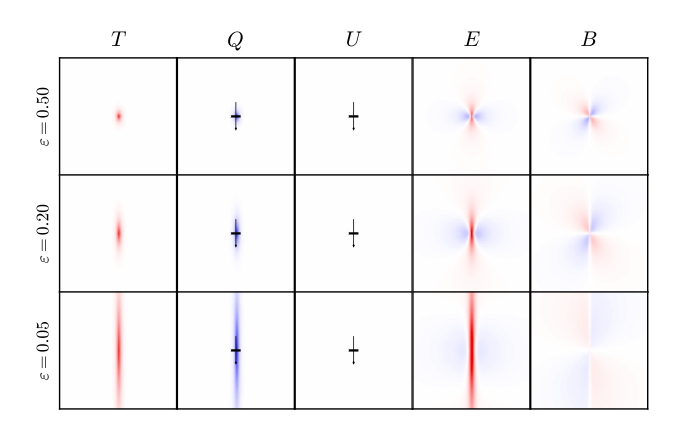


Figure 1. Stokes parameters and scalar polarization quantities for idealized filaments as we alter the aspect ratio. The magnetic field (thin arrow) is vertical, so the polarization direction is horizontal (thick line), making Q<0 and U=0. In sky convention, north is to the top and east is to the left. The filaments are 2, 5, and 20 times longer than they are wide (axis ratio $\epsilon=0.5,0.2,0.05$). Scalars E and E are on the same color scale, which has half the range of the E scale. The E scale differs from E by an arbitrary polarization fraction

Working in the flat sky approximation, the Fourier components of the scalar polarization modes are:

$$(E+iB)(\ell) = \exp(-2i\phi_{\ell})X(\ell). \tag{3}$$

Fig. 1 shows the Stokes T, Q, U and scalar E, B quantities on the sky for sample, north-south filaments with $\psi_{\rm pol} = 90^{\circ}$, so the magnetic field is parallel to the filament direction and the polarization is perpendicular. (Our choice of coordinates implies that Stokes U is zero in these cases.) When the magnetic field aligns with the filament direction, Rotti & Huffenberger (2019) pointed out that the real-space kernels for the E/B signals show immediately that the E-type polarization is positive along the filament, regardless of its orientation. Since the temperature signal is also strong there, such filaments naturally yields a strong and positive TE crosscorrelation, as observed in the Planck data. The same work showed that the B signal is concentrated at the ends of the filament, so filaments with long and thin aspect ratios will have less B power relative to E power than more squat ones.

By parity symmetry, the TB and EB cross-correlations are zero when the polarization is perpendicular to the filament (i.e. $\psi_{\rm pol} = 90^{\circ}$). In Fig. 2 we show how the E and B patterns transform into each other (and change sign) as $\psi_{\rm pol}$ varies away from 90° . In these cases, the TB and EB correlation can be non-zero for individual filaments, but so long as the average $\langle \psi_{\rm pol} \rangle = 90^{\circ}$,

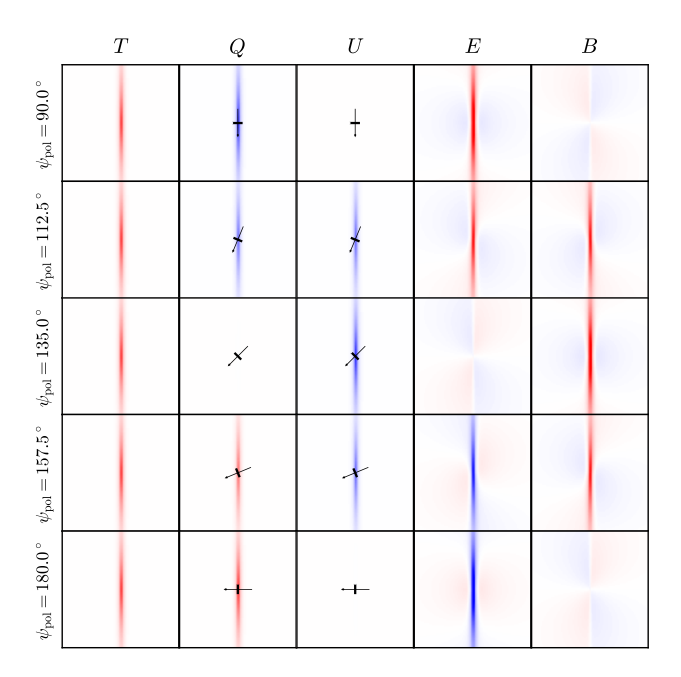


Figure 2. Like Fig. 1, but showing the polarization quantities as we alter the magnetic field direction (and hence the polarization angle), for a fixed filament orientation. The Q and U Stokes parameters follow HEALPix polarization convention for a north–south filament, but the E and B fields are coordinate independent and appropriate for any orientation. Note that filaments with aligned magnetic fields ($\psi_{\rm pol}=90^{\circ}$) have zero TB correlation. Filaments with relative polarization angles $90^{\circ} < \psi_{\rm pol} < 180^{\circ}$ have positive TB correlations, as depicted, while those with $0^{\circ} < \psi_{\rm pol} < 90^{\circ}$ have negative TB correlations (not shown).

there will be no overall cross-correlation for the whole population.

2.1. Projection on the sky

We next discuss the projection of a three-dimensional filament onto the plane of the sky. Many important quantities depend on the angle to the line of sight of (1) the long axis of the filament (θ_L) and (2) the magnetic field vector (θ_H) . Another important quantity is the the plane-of-sky projection of the angle between these vectors (ψ_{LH}) , which controls the polarization angle and the amounts of E/B polarization present. We depict these angles in Fig. 3. If the magnetic field direction aligns somewhat with the filament direction, as is the case in strong-field MHD, all these angles will be correlated.

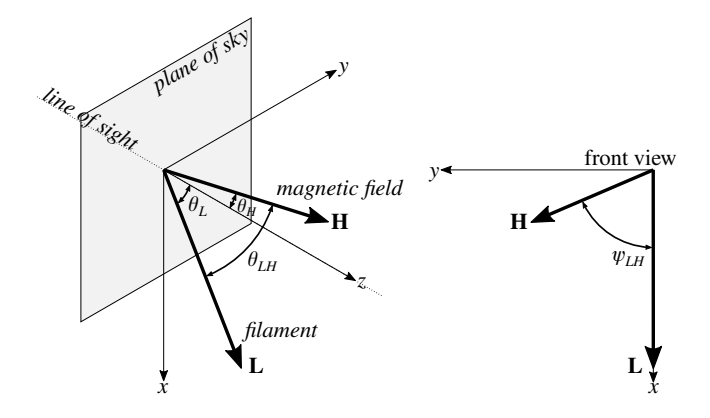


Figure 3. Geometry of the filament direction and the magnetic field. The long axis of the filament \mathbf{L} points in the x-z plane at an angle θ_L from the line of sight. The magnetic field \mathbf{H} has an angle from the line of sight of θ_H . The angular misalignment between the field and the filament is θ_{LH} . The front view gives the projection of the misalignment onto the plane of the sky, ψ_{LH} .

We assume that on average, the filaments align with the local magnetic field. In the appendix, we use simple geometry to compute the distribution of the magnetic field projection angle θ_H and relative orientation angle ψ_{LH} as a function of θ_L . We base the distribution on the assumption of a Gaussian distribution for the angle (θ_{LH}) between the filament and the magnetic field in three dimensions, characterized by the dispersion RMS (θ_{LH}) .

The field angle θ_H is correlated with ψ_{LH} , so our numerical procedure yields the tabulated joint distribution,

$$p(\psi_{LH}, \theta_H | \theta_L).$$
 (4)

This distribution centers on aligned filaments ($\psi_{LH} = 0^{\circ}, \theta_{H} = \theta_{L}$), and the distribution for ψ_{LH} broadens for filaments nearly along the line of sight. Its precise form is not vital for this discussion and is plotted in the appendix in Fig. 8.

On the other hand, the probability distribution for the line-of-sight angle of randomly oriented filaments is determined purely by geometry,

$$p(\theta_L) = \sin \theta_L,\tag{5}$$

for $\theta_L \in [0, 180^{\circ}]$.

These quantities relate immediately to the polarization. Although the dust polarization fraction depends on the microphysical details of the emission, it has a geometric dependence like $f_{\rm pol} \propto \sin^2 \theta_H$ (Fiege & Pudritz 2000). Meanwhile, the polarization angle for a filament projected along the x-axis is $\psi_{\rm pol} = \psi_{LH} + 90^{\circ}$.

We model the filament as a prolate spheroid, and label the major axis as L_a and the minor axis as L_b . The

 $^{^1}$ Elsewhere in the ISM literature, the angles are often given with reference to the plane of the sky, e.g. $\gamma_H=90^\circ-\theta_H$ and so on.

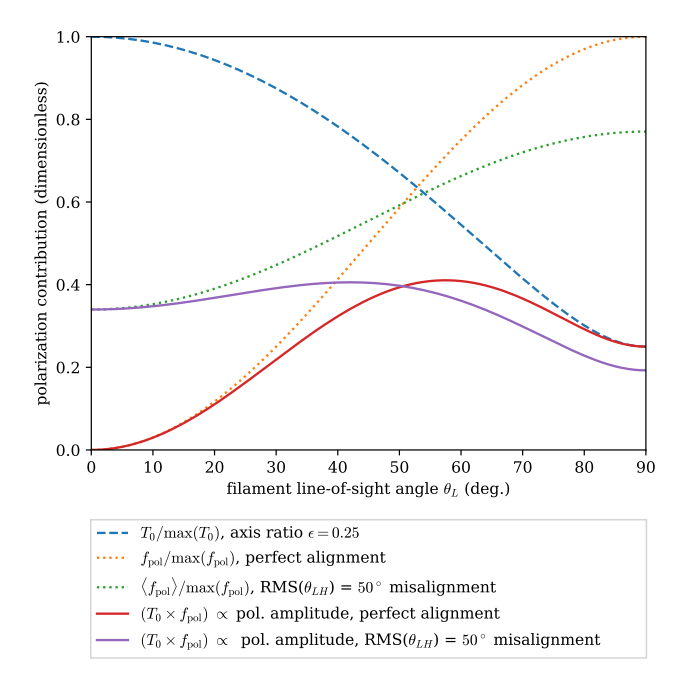


Figure 4. Total intensity, polarization fraction, and polarization amplitude dependence on the filament orientation. Filament oriented along the line of sight have $\theta_L = 0^{\circ}$, while filaments in the plane of the sky have $\theta_L = 90^{\circ}$. The filament is modeled with an axis ratio $\epsilon = 0.25$, and the filament direction (θ_L) and the magnetic field direction (θ_H) are either perfectly aligned or stochastically misaligned in three-dimensions.

axis ratio is thus $\epsilon = L_b/L_a < 1$. The column density (and therefore the surface brightness and ultimately the observed temperature perturbation) is proportional to the density and the line of sight distance through the filament, and so (approximately)

$$T_0 \propto \rho_0 \left(L_a^2 \cos^2 \theta_L + L_b^2 \sin^2 \theta_L \right)^{1/2}$$

$$\propto \rho_0 L_a \left(\cos^2 \theta_L + \epsilon^2 \sin^2 \theta_L \right)^{1/2},$$
(6)

where ρ_0 is a characteristic density for the filament. So all else being equal, a filament that lies along the line of sight will have the greatest column density and the brightest temperature signal. On the other hand, $f_{\rm pol} \propto \sin^2\theta_H$, so if the magnetic field lies along the line-of-sight, there is no polarization. The polarization fraction is maximum when the magnetic field is perpendicular to the line of sight.

Fig. 4 relates the column density and polarization fraction effects of the line-of-sight angle. It also shows that since the polarized amplitude depends on the product of these two, the filaments with the brightest polarization are inclined, but not perpendicular, to the line of sight. The polarization maximum depends on axis ratio through its impact on the column density. Nearly

round filaments have the polarization maximum when oriented near 90° to the line of sight, while in the limit of thin filaments ($\epsilon \to 0$) the polarization maximum orientation approaches $\theta_L = 45^\circ$ for perfect magnetic field alignment. If there is significant misalignment of the magnetic field and filament directions, the situation can become more complicated, depending on the particular combination of axis ratio and misalignment dispersion. In such cases, filaments along the line of sight can have significant polarization. Still, the typical line-of-sight orientation angle for maximum polarization, averaging over the magnetic field directions, is around $\theta_L = 45^\circ$.

We compute the filament's projected angular sizes along its two axes as if it were a cylinder. These depend on its distance R and are:

$$\Theta_a = \left(L_a^2 \sin^2 \theta_L + L_b^2 \cos^2 \theta_L\right)^{1/2} / R$$

$$= \left(\sin^2 \theta_L + \epsilon^2 \cos^2 \theta_L\right)^{1/2} L_a / R$$

$$\Theta_b = L_b / R = \epsilon L_a / R.$$
(7)

Thus the projected axis ratio is

$$\epsilon_{\Theta} = \Theta_b / \Theta_a = \frac{\epsilon}{\left(\sin^2 \theta_L + \epsilon^2 \cos^2 \theta_L\right)^{1/2}}$$
(8)

which goes to unity for filaments along the line of sight, and to the true value (ϵ) for filaments perpendicular to the line of sight.

2.2. Filaments in Fourier space

For several terms in our power spectrum calculation, we need the Fourier transform of the projected filament profile:

$$f(\ell) = \int d^2x \ f(\mathbf{x}) \exp(-i\ell \cdot \mathbf{x}).$$
 (9)

Rather than project rays through a 3-dimensional model to obtain the filament profile, we make a simplifying assumption for computational efficiency. From the size and orientation of a filament, we take the angular dimensions and compute under the assumption that the profile is a distortion from an axisymmetric function g:

$$f(x,y) = g(x/\Theta_a, y/\Theta_b)$$

$$= g(x^*, y^*) = g(r)$$
(10)

where Θ_a, Θ_b are the semi-major and semi-minor axis of the elliptical distortion. As we stated, by convention and without loss of generality, we orient the long axis of the filament along the x-axis.

Then the transform of f is simply related to the transform of g:

$$f(\ell) = \Theta_a \Theta_b \int d^2 x^* \ g(\mathbf{x}^*) \exp(-i(\Theta_a \ell_x x^* + \Theta_b \ell_y y^*))$$
$$= \Theta_a \Theta_b \ g(\ell^*) \tag{11}$$

where $\ell^*(\ell) = (\Theta_a^2 \ell_x^2 + \Theta_b^2 \ell_y^2)^{1/2}$ and

$$g(\ell^*) = \int d^2x^* \ g(\mathbf{x}^*) \exp(i\boldsymbol{\ell}^* \cdot \mathbf{x}^*)$$

$$= 2\pi \int dr \ r \ g(r) J_0(\ell^* r).$$
(12)

The input profile $g(\mathbf{x}^*)$ is real and even, and so the Fourier transform is too. The power spectra we find are not very sensitive to the profile that we use. In this work we have used an exponential for the basic filament profile $(g(r) = \exp(-r))$, but we have checked our best-fitting power spectrum model with a Gaussian profile $(g(r) = \exp(-r^2/2))$ and a Plummer profile $(g(r) = (1 + r^2)^{-5/2})$, and find the same results.

2.3. Parameters and one-filament term

For a parameterized set of filament properties,

$$\alpha = (L_a, L_b, \psi_{LH}, \theta_L, \theta_H, R, \dots),$$

we can write the number density distribution $n(\alpha)$, so that the average number of filaments in a realization of the sky is

$$\langle N \rangle = \int d\Omega \ d\alpha \ n(\alpha) \tag{13}$$

where the integral is over

$$d\alpha = dL_a dL_b d\psi_{LH} d\theta_H d\theta_L dR. \tag{14}$$

Expressed another way, $n(\alpha) = \langle N \rangle p(\alpha)$, where the normalized probability distribution of the filament population is

$$p(\alpha) = p(L_a, L_b)p(\psi_{LH}, \theta_H | \theta_L)p(\theta_L)p(R)$$
 (15)

This integral over the population is at least six dimensional. For a screen at a distance R, it is five dimensional integral. Since the angular power spectrum for foregrounds is a power law, if we can reproduce it on a single screen, putting that screen at different distances will maintain the same power spectrum. If we further fix the physical aspect ratio of the filaments, it is a four dimensional integral, over $L_a, \psi_{LH}, \theta_L, \theta_H$. (The projected aspect ratio will still vary with the line-of-sight angle θ_L .)

The power spectrum contributions from filaments correlated with themselves are:

$$C_{\ell}^{TT} = \frac{1}{2\pi} \int d\phi_{\ell} \int d\alpha \ n(\alpha) \ |T(\ell, \alpha)|^{2}, \tag{16}$$

$$C_{\ell}^{EE} = \frac{1}{2\pi} \int d\phi_{\ell} \int d\alpha \ n(\alpha) \ |E(\ell, \alpha)|^{2},$$

$$C_{\ell}^{BB} = \frac{1}{2\pi} \int d\phi_{\ell} \int d\alpha \ n(\alpha) \ |B(\ell, \alpha)|^{2},$$

$$C_{\ell}^{TE} = \frac{1}{2\pi} \int d\phi_{\ell} \int d\alpha \ n(\alpha) \ T(\ell, \alpha) E(\ell, \alpha)^{*}.$$

Similar expressions hold for the other cross correlations, but these vanish if the orientations of the filaments are random. These power spectra computations are directly analogous to the 1-halo term in the cosmological halo model (Seljak 2000).

3. RESULTS

There are clear relationships between the physical properties of the filaments and the temperature and polarization power spectra that they produce. The slopes of the power spectra are determined primarily by the size distribution of filaments, with other effects responsible for the smaller differences between the components. The ratio of BB/EE power is determined mostly by the aspect ratio of the filaments and somewhat by the misalignment of the filament directions to the background magnetic field. These same factors also determine the cross correlation r_{ℓ}^{TE} , but here misalignment is much more important. They also affect the TE/EE power ratio, but this quantity is more directly affected by the overall polarization fraction.

3.1. Power spectrum shape

We can relate the slope of a power law spectrum to scaling relations for parameters in the filament profiles. This allows us to place constraints on the distribution of filament sizes and the scaling of other parameters. For a generic parameter α_0 , if the filament's contribution to the power spectrum scales as

$$C_{\ell} \propto \int d\alpha_0 \ n(\alpha_0) \times \alpha_0^q F(\alpha_0^r \ell)$$
 (17)

for any function F, and furthermore if the weighting distribution for the parameter is a power law, $n(\alpha_0) \propto \alpha_0^p$, then we can rescale the integration with a straightforward substitution, $u = \alpha_0 \ell^{1/r}$:

$$C_{\ell} \propto \ell^{-(p+q+1)/r} \times$$

$$\int d(\alpha_0 \ell^{1/r}) (\alpha_0 \ell^{1/r})^p \times (\alpha_0 \ell^{1/r})^q F((\alpha_0 \ell^{1/r})^r)$$

$$\propto \ell^{-(p+q+1)/r} \times \int du \ u^p u^q F(u^r).$$
(18)

The integral no longer has any multipole dependence and evaluates to some constant value, whatever the details of F. Thus we are left with a powerlaw power spectrum with

$$C_{\ell} \propto \ell^{-(p+q+1)/r}$$
 (19)

This argument holds not just for filaments, but for any signal with a power-law power spectrum that is built from a set of objects that are similarly related to each

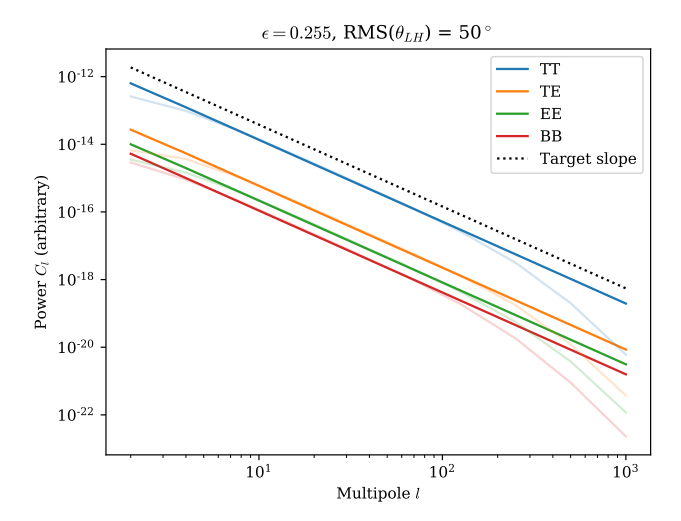


Figure 5. Power spectra slopes of temperature and polarization are set chiefly by the distribution of filament lengths, which has been chosen here so that the slopes match the dotted line, $C_{\ell} \propto \ell^{-2.4}$. The ratios between the power spectra are set by the overall polarization fraction, the aspect ratio of filaments, and the misalignment between the filaments and their local magnetic field. When maximum and minimum sizes truncate the distribution of the filaments, the power falls below the targeted slope (semi-transparent colors).

other, so long as they are weighted by powerlaw scalings and distributions. So if we observe a powerlaw spectrum with $C_{\ell} \propto \ell^s$, it implies that the parameter distribution's index is p = -rs - q - 1, regardless of the objects' profiles.

We walk through this scaling argument for a simple (and unrealistic) case—with plane-of-sky filaments with identical surface brightnesses (T_0 is the same for all filaments) and a constant projected-axis-ratio ($\Theta_b = \epsilon \Theta_a$)—and analyze the distribution for Θ_a , the angular size of filaments. For the filament Fourier transform, we have $f(\ell) \propto \Theta_a^2 g(\ell^*)$ with $\ell^* \propto \Theta_a$. The power spectrum contribution is proportional to f^2 , so comparing the scaling for angular size parameter Θ_a to equation 17, we find q=4 and r=1. In the polarization case, to reproduce $C_\ell \propto \ell^{-2.4}$ (meaning s=-2.4), the number density distribution of such objects on the sky must approximately scale like $n(\Theta_a) \propto \Theta_a^p$ where p=2.4-4-1=-2.6. Indeed this yields the desired power spectrum slope when calculated in our model.

In a more realistic case, with three-dimensional filaments, we can make a similar argument to deduce the distribution of filament lengths. Surface brightness depends on column density, which is proportional to length (after integrating out any distribution of axis ratios—compare equation 7—and assuming a density normalization independent of length). The solid angle scales

like length squared. After squaring those three powers during the computation of the power spectrum, the overall scaling is q=6. The multipole ℓ scaling should also go like length, so r=1, the same as the plane-of-sky case above. So with no other dependence on length, we should have distribution of lengths $n(L_a) \propto (L_a)^p$ where $p=2.4-6-1=-4.6.^2$

We have verified that this distribution produces the proper slope in Fig. 5. All the temperature and polarization spectra have the specified slope in common. The complications of the modeling of the three dimensional orientation are not important to the slope, only the weighting and distribution of filament size.

Other than the slope, there are not clear features in the Planck-measured spectra. We note that features in the distribution of filament sizes would break the powerlaw behavior of the resulting spectra. For example, if we impose a maximum filament size (semi-transparent lines in Fig. 5), it causes the low- ℓ behavior of C_{ℓ} to deviate: at scales much larger than the filament, the temperature spectrum adopts the flat, white, Poisson spectrum of point sources. The EE and BB spectra flatten the same way, and on scales large compared to the filaments, the aspect ratios of the filaments become unimportant and the amount of power in EE and BB equalize. The TE cross-correlation falls off at large scales, possibly because the positive and negative contributions to E are being averaged over. If, on the other hand, we impose a minimum filament size, it causes the high-ℓ behavior to deviate: the spectrum will drop off with increasing ℓ , where there is no more contribution to the power.

In yet more realistic cases, we can make the slopes of all the temperature and polarization spectra differ. For example, this can happen if there is another effect that changes the size scaling of the polarization relative to the temperature. For example, to make polarization slope shallower than the temperature slope, one could make smaller objects more polarized than large objects, or if the aspect ratio of filaments changes as a function of size.

Considering the Planck data, it is not immediately clear what conclusion to draw. Planck Collaboration et al. (2018) quote EE, BB, TE slopes for the dust foreground, but not the TT slope. Using our own tools, we have computed the TT power spectrum based on the Planck data, and find a TT slope that is about -2.6,

² If the column density normalization depends on length, this procedure yields a net distribution that is a product of the size distribution and the density squared distribution (both as a function of length). Such a case could arise, for example, if small filaments are collapsed versions of large ones and have higher density.

somewhat steeper than the polarization spectra at -2.4 to -2.5. Like Planck Collaboration et al. (2018), for the mask we used the LR71 polarization mask supplemented with a point source mask (based on intensity maps), resulting in a mask with effective $f_{\rm sky} \simeq 0.6$. We can approximately reproduce a -2.6 temperature slope and -2.4 polarization slope with $n(L_a) \propto L_a^{-4.4}$ and $f_{\rm pol} \propto L_a^{-0.08}$. This argues that in the unmasked region, the polarization is higher in smaller filaments.

However, this conclusion may not be correct because it depends sensitively on the mask. We reasoned that small filaments, oriented along the line of sight, might look like a point source and be included in the masked area. These end-on filaments could also have low polarization (note Fig. 4), and excluding them might not have much effect on the polarization results. Thus for comparison, we recomputed the TT spectrum with different masks. When we use only the polarization LR71 mask without removing the additional point sources from the intensity map, we get a shallower TT spectrum with slope -2.5. When we use a mask that keeps the same large scale features but does not mask any point sources (Planck's publicly available GAL70 mask) we find a TTslope of -2.1, notably shallower than the polarization spectra. The polarization spectra change somewhat between these masks, but the changes in the polarization slopes are small compared to the change in the TT slopes. Some of the masked sources are extragalactic, so this slope with all point sources unmasked is probably too shallow to describe the ISM component, but can serve as a bound. The upshot is that we are not certain whether the spectrum for all filaments is steeper or shallower in temperature than polarization, and so it is difficult to draw conclusions on the size dependence of the polarization fraction.

Another feature of the Planck data is the differing slopes in E and B. We can reproduce this feature by varying the aspect ratio as a function of filament size. For the LR71 mask in Planck Collaboration et al. (2018), the slopes for (BB, EE, TE) are roughly (-2.5, -2.4, -2.5) and we found a TT slope of -2.6. So BB is steeper than EE, which should happen if smaller filaments are proportionally thinner than longer ones. Modifying the aspect ratio in this way also affects the TT slope, breaking the simple relation that we saw earlier in this section. By trial and error, we found that this set of slopes are approximately reproduced with the following parameter dependence: $\epsilon \propto L_a^{0.1}, \, n(L_a) \propto L_a^{-4.45}, \, {\rm and} \, f_{\rm pol} \propto L_a^{-0.1}.$ Here we are simply exploring what is possible, but the relationship between the measured slopes and these filament parameters should be made more systematic and quantitative.

In light of these complications and uncertainties, in what follows we keep a common slope of -2.4 for all the temperature and polarization components while we explore their other parameter dependences.

3.2. BB/EE power ratio

The aspect ratio of the filaments is the major factor determining the ratio of B-mode power to E-mode power. In Fig. 6, we plot the power ratio against the aspect ratio for varying degrees of filament–magnetic field misalignment. To reproduce the Planck-observed ratio of ~ 0.5 , filaments need to have an aspect ratio ϵ slightly less than 0.26, so filaments must be slightly less than four times longer than they are wide. If the model deviates too much from this ratio, the required magnetic field misalignment is made so large that the model has trouble fitting the TE correlation.

It is difficult to compare this result quantitatively to the aspect ratios of observed filaments from the literature without making a detailed accounting of the filament selection function. Projection effects will also tend to lower observed aspect ratios. The stacked filaments in Fig. 7 of Planck Collaboration et al. (2016b) appear to have axis ratios not so far from what we are finding here. The filaments identified by the Rolling Hough transformation in Clark et al. (2014) on HI maps tend to be longer and thinner than this.

3.3. TE cross-correlation

In the context of the filament model, we find that the level of the TE cross correlation implies that filaments cannot be precisely aligned to their local magnetic field direction. The correlation coefficient is defined as

$$r_{\ell}^{TE} = C_{\ell}^{TE} / \sqrt{C_{\ell}^{EE} C_{\ell}^{TT}}, \qquad (20)$$

and perfect alignment of the filaments and the fields causes far too much TE correlation compared to the Planck observations.

The Planck dust data show $r_\ell^{TE} \approx 0.35$ with little scale dependence (Planck Collaboration et al. 2018). Fig. 7 shows that to match this, the field misalignment angle θ_{LH} must have an RMS dispersion of nearly 50°, while maintaining the axis ratio $\epsilon \approx 0.26$ needed to reproduce the BB/EE power ratio. If the misalignment dispersion is independent of filament size, as in our modeling, it causes no scale dependence: r_ℓ^{TE} is constant.

Projection effects cause the distribution of the projected angle ψ_{LH} to have a positive kurtosis (see appendix, Fig. 10), and so we can describe its dispersion in a few ways. For the RMS(θ_{LH}) = 50° case, 68 percent of the probability is bounded by $|\psi_{LH}| < 45^{\circ}$. Alternatively, $[\text{Var}(\psi_{LH})]^{1/2} = 48^{\circ}$. For comparison, Planck

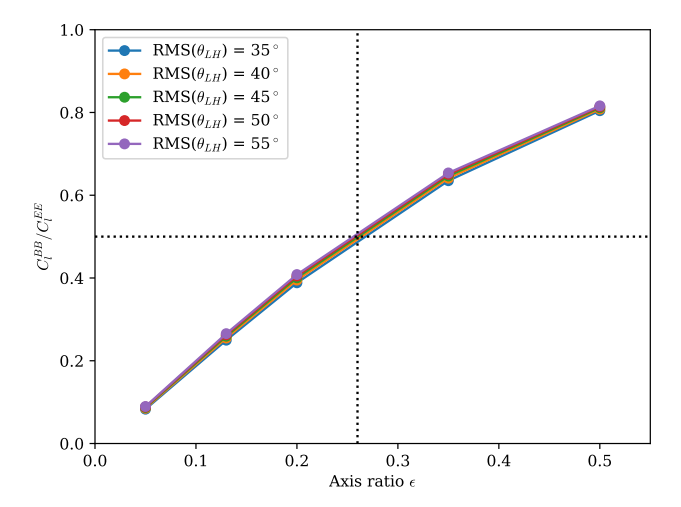


Figure 6. Ratios of BB to EE power as a function of the physical filament axis ratio. Long and thin filaments (ϵ small) have less B-mode power than E-mode power. Short and squat filaments (aspect ratio ϵ close to unity) have B power close to the E power. An aspect ratio of about $\epsilon = 0.26$ can reproduce the Planck-observed ratio of about one half, but this can be traded off against a slight dependence with the dispersion in the misalignment angle θ_{LH} between the filament direction and the magnetic field direction in three dimensions.

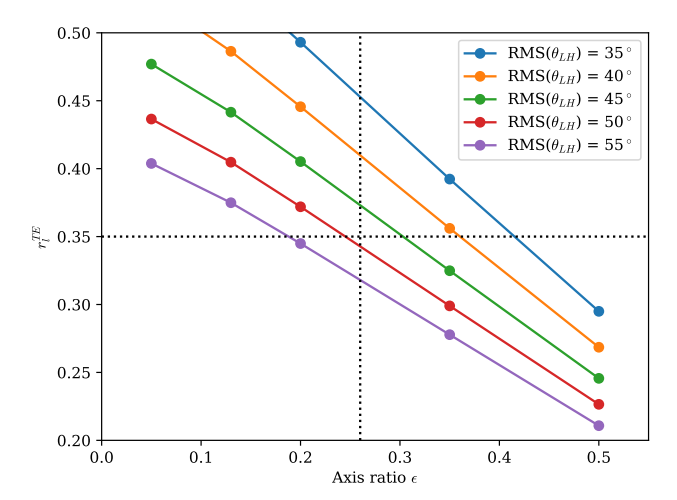


Figure 7. Correlation coefficient of TE power as a function of the axis ratio. Thinner filaments (small ϵ) have stronger TE correlations for various magnetic field–filament misalignments. Since the B-to-E power ratio requires $\epsilon \approx 0.26$ (Figure 6), the TE correlation is diagnostic of the misalignment necessary to produce the Planck-observed $r^{TE} \approx 0.35$, which needs $RMS(\theta_{LH}) \approx 50^{\circ}$.

Collaboration et al. (2016b) fit a Gaussian a with 19° dispersion (1σ) to the projected field–projected filament histogram of relative orientations for the filaments they found. Again this comparison is not direct because of selection effects. Their Hessian-based selection of filaments would disfavor filaments with small projected aspect ratios (close to the line of sight), and such filaments can have the largest differences in the projected orientation.

The overall level of C_{ℓ}^{TE} (and the polarization spectra) depends on the polarization fraction. The relative power ratio has a dependence like

$$C_{\ell}^{TE}/C_{\ell}^{EE} \propto \langle f_{\rm pol} \rangle / \langle f_{\rm pol}^2 \rangle,$$
 (21)

while for the cross correlation it is

$$r_{\ell}^{TE} \propto \langle f_{\rm pol} \rangle / \langle f_{\rm pol}^2 \rangle^{1/2}.$$
 (22)

Thus a purely multiplicative rescaling of the polarization fraction affects the ratios of the power in TT/TE/EE but not the correlation coefficient r^{TE} .

To reproduce the Planck-measure ratio $C_\ell^{TE}/C_\ell^{EE}\sim 2.7$ (in our case that already fits C_ℓ^{BB}/C_ℓ^{EE} and r_ℓ^{TE}) requires $f_{\rm pol}=0.15\,\sin^2\theta_H$. We have only modeled the polarization fraction amplitude and the geometric dependence on the magnetic field orientation, but in addition, the polarization fraction depends on grain geometry and small-scale turbulence (Fiege & Pudritz 2000), and filaments need not in reality have all the same intrinsic polarization fraction.

Our other tests have shown that the TE correlations differ in their sensitive to intrinsic dispersion in the polarization fraction. For example, the correlation r^{TE} is not very sensitive to the maximum polarization fraction, but the power ratio is very sensitive to it: decreasing the maximum polarization fraction decreases C_ℓ^{TE} but decreases the denominator C_ℓ^{EE} more, and so raises the ratio.

3.4. Parity violation: TB and EB

One surprising finding in the Planck Collaboration et al. (2018) dust spectra is a non-zero TB correlation, with $r_\ell^{TB} \approx 0.05$. Like r^{TE} , the observed r^{TB} correlation has little scale dependence (up to multipoles of several hundred).

Because non-zero TB and EB are parity-violating correlations, our model cannot reproduce them for randomly-oriented filaments. To get a positive TB correlation we would need to favor polarization angles in the range $\psi_{\rm pol} \in [90^{\circ}, 180^{\circ}]$ relative to the filament direction (compare Fig. 2). Equivalently, this corresponds to projected field angles in the range $\psi_{LH} \in [0^{\circ}, 90^{\circ}]$.

Such an effect may be due to some large scale feature in the Galaxy's magnetic field or differential gas flow (e.g. Planck Collaboration et al. 2018; Bracco et al. 2019).

We can determine how far away from random this correlation is by artificially weighting the distribution of the projected misalignment angles, favoring the $\psi_{LH}>0$ portion of the distribution of $p(\psi_{LH},\theta_H|\theta_L)$ over the $\psi_{LH}<0$ portion, while keeping the same functional form. We find that we can approximately reproduce the Planck measured TB correlation by giving the preferred ψ_{LH} directions about 55 percent of the total weight, rather than the 50 percent than comes naturally from randomly oriented filaments. Similar to the r^{TE} correlation (also set by field–filament misalignment), this effect is not scale dependent, and so r^{TB} is constant to high ℓ in this model.

Our modeling comes from the 1-halo term only, and shows that the TB correlation can be explained if filaments orientations in projection are slightly twisted counterclockwise from the projected local magnetic field. Our model does not address the structure of that underlying field, but we may speculate that some differential, shearing hydrodynamic forcing could preferentially twist the filaments, according to our point of view, from the global mean field direction of the Milky way.

Bracco et al. (2019), argue that the observed TE and TB correlations may be features of the large scale structure of the Galactic magnetic field. They show that a helical component can create such correlations, but in their modeling, the correlation show a strong scale dependence, with $r_{\ell}^{TE,TB}$ falling substantially already by $\ell=22$. The Planck spectra have much flatter $r_{\ell}^{TE,TB}$ correlations, consistent with the filament modeling here.

Planck did not detect an EB correlation, but since E and B both have a factor of the polarization fraction, we would naturally expect this correlation to be smaller. It may be there, hidden in the noise. In the presence of a positive TB correlation, in the context of the filament modeling, we would expect a positive EB correlation too (including at high- ℓ), and it should be a target for future experiments. Both TB and EB dust correlations can potentially interfere with sky-calibration of the polarization angles of CMB-instruments (Abitbol et al. 2016) or with CMB lensing reconstruction (e.g. Fantaye et al. 2012; Challinor et al. 2018).

4. CONCLUSIONS

We do not know how much of the dusty microwave polarization foreground is due to filamentary structure, but if it is a substantial portion, we can discern details of the filament population from the foreground power spectra. We showed that the slopes of the power spectra relate to the distribution of lengths. We showed that the BB/EE power ratio relates to the filament axis ratio. We showed that the TE cross-correlation relates to the axis ratio and the RMS misalignment of filaments to the magnetic field. We showed that TB correlations could be caused by a slight preference for one handedness in the misalignment between the magnetic field and the filament orientation.

Despite its relative success in reproducing the features of the dust polarization power spectrum, this formalism lacks some essential features for modeling the real sky. Foremost, it begins with the assumption of a population of filaments, which is not itself on a firm physical basis, and which may not be a unique way to explain the features in the foreground polarization power spectra. Even in the context of filaments, this formalism includes only the one-filament term in the power spectra. This is obviously an approximation, for the Planck data have shown that the Galaxy's projected magnetic field has coherent, large-scale features, and the HI-identified filaments are clearly correlated with it and with starlight polarization measurements (Clark et al. 2015). On the other hand, in the halo model, the transition from one-halo-dominated to two-halo-dominated scales often leaves a mark on the power spectrum. Since in the dust polarization spectra there are not clear features, like a break in the slope, we may speculate that the two-halo component may not be necessary to describe the main properties of the power spectra. Inclusion of a proper two-halo formalism is complicated by the correlated direction dependence of the filaments. We may be able to import some of the techniques developed to describe galaxy intrinsic alignments (e.g Schneider & Bridle 2010), since the mathematical description of the problem is similar.

We have not tried to systematically probe the parameter degeneracies or place proper uncertainties on any of the parameters of this filament model. We can do this straightforwardly by interfacing the model with a Monte Carlo Markov Chain and developing a likelihood based on the Planck dust spectra. We plan to pursue this in further work.

By looking at observations and simulations of the filamentary ISM, we could attempt to verify some of the population statistics for filaments. For example, we could compare the length distribution of actual or simulated filaments to that implied by the slope of the power spectra.

Because this filament model is non-Gaussian, we may be able to use it to design novel diagnostics to probe for residual foregrounds in surveys that aim for the primordial *B*-modes (in the spirit of Kamionkowski & Kovetz 2014; Rotti & Huffenberger 2016; Philcox et al. 2018; Coulton & Spergel 2019). Similarly, we could use this model to compute the four-point contributions to polarized CMB lensing estimators. This could help place constraints on potential foreground contamination. Such statistics may be sensitive to the internal density structure of the filaments in a way that the power spectrum is not.

Due to its flexibility, its ability to model the Planck dust polarization data, its ease of computation, and its straightforward interpretation, this filament model may become a useful tool in the study of CMB polarization foregrounds.

ACKNOWLEDGMENTS

KMH, AR, and DCC acknowledge support from the NASA ATP program under grant NNX17AF87G. KMH acknowledges support from the NSF AAG program under grant 1815887. AR acknowledges support from the European Research Council (ERC) under the European Union's Horizon 2020 research and innovation programme (grant agreement No 725456, CMBSPEC). We thank J. Colin Hill, Susan Clark, Marc Kamionkowski, and Carlos Hervias-Caimapo for useful conversations. We thank Francois Boulanger for providing access to masks used in the Planck Collaboration et al. (2018) analysis. The anonymous referee provided useful suggestions for placing this work in the context of the turbulent ISM.

REFERENCES

Abazajian, K. N., Adshead, P., Ahmed, Z., et al. 2016, arXiv e-prints, arXiv:1610.02743. https://arxiv.org/abs/1610.02743

Abitbol, M. H., Hill, J. C., & Johnson, B. R. 2016, MNRAS, 457, 1796, doi: 10.1093/mnras/stw030

Beattie, J. R., Federrath, C., & Klessen, R. S. 2019, MNRAS, 487, 2070, doi: 10.1093/mnras/stz1416

Bracco, A., Candelaresi, S., Del Sordo, F., & Brandenburg, A. 2019, A&A, 621, A97,

doi: 10.1051/0004-6361/201833961

Brandenburg, A., & Lazarian, A. 2013, SSRv, 178, 163, doi: 10.1007/s11214-013-0009-3

Burkhart, B., Stanimirović, S., Lazarian, A., & Kowal, G. 2010, ApJ, 708, 1204,

doi: 10.1088/0004-637X/708/2/1204

Caldwell, R. R., Hirata, C., & Kamionkowski, M. 2017, ApJ, 839, 91, doi: 10.3847/1538-4357/aa679c

Challinor, A., Allison, R., Carron, J., et al. 2018, Journal of Cosmology and Astro-Particle Physics, 2018, 018, doi: 10.1088/1475-7516/2018/04/018

Clark, S. E., & Hensley, B. S. 2019, ApJ, 887, 136, doi: 10.3847/1538-4357/ab5803

Clark, S. E., Hill, J. C., Peek, J. E. G., Putman, M. E., & Babler, B. L. 2015, PhRvL, 115, 241302, doi: 10.1103/PhysRevLett.115.241302

Clark, S. E., Peek, J. E. G., & Putman, M. E. 2014, ApJ, 789, 82, doi: 10.1088/0004-637X/789/1/82

Cooray, A., & Sheth, R. 2002, PhR, 372, 1, doi: 10.1016/S0370-1573(02)00276-4

Coulton, W. R., & Spergel, D. N. 2019, JCAP, 2019, 056, doi: 10.1088/1475-7516/2019/10/056 de Avillez, M. A., & Breitschwerdt, D. 2005, A&A, 436, 585, doi: 10.1051/0004-6361:20042146

Elmegreen, B. G., & Scalo, J. 2004, Annual Review of Astronomy and Astrophysics, 42, 211, doi: 10.1146/annurev.astro.41.011802.094859

Fantaye, Y., Baccigalupi, C., Leach, S. M., & Yadav, A. P. S. 2012, Journal of Cosmology and Astro-Particle Physics, 2012, 017, doi: 10.1088/1475-7516/2012/12/017

Fiege, J. D., & Pudritz, R. E. 2000, ApJ, 544, 830, doi: 10.1086/317228

Goldreich, P., & Sridhar, S. 1995, ApJ, 438, 763, doi: 10.1086/175121

Górski, K. M., Hivon, E., Banday, A. J., et al. 2005, ApJ, 622, 759, doi: 10.1086/427976

Hanany, S., Alvarez, M., Artis, E., et al. 2019, arXiv e-prints, arXiv:1902.10541.

https://arxiv.org/abs/1902.10541

Heiles, C., & Haverkorn, M. 2012, SSRv, 166, 293, doi: 10.1007/s11214-012-9866-4

Hennebelle, P. 2013, A&A, 556, A153, doi: 10.1051/0004-6361/201321292

Hervías-Caimapo, C., Bonaldi, A., & Brown, M. L. 2016, MNRAS, 462, 2063, doi: 10.1093/mnras/stw1787

Hu, Y., Yuen, K. H., & Lazarian, A. 2020, ApJ, 888, 96, doi: 10.3847/1538-4357/ab60a5

Kalberla, P. M. W., Kerp, J., Haud, U., et al. 2016, ApJ, 821, 117, doi: 10.3847/0004-637X/821/2/117

Kamionkowski, M., & Kovetz, E. D. 2014, PhRvL, 113, 191303, doi: 10.1103/PhysRevLett.113.191303

Kandel, D., Lazarian, A., & Pogosyan, D. 2017, MNRAS, 472, L10, doi: 10.1093/mnrasl/slx128

—. 2018, MNRAS, 478, 530, doi: 10.1093/mnras/sty1115

- Kim, C.-G., Choi, S. K., & Flauger, R. 2019, ApJ, 880, 106, doi: 10.3847/1538-4357/ab29f2
- Kritsuk, A. G., Flauger, R., & Ustyugov, S. D. 2018, $\label{eq:phRvL} PhRvL,\,121,\,021104,$

doi: 10.1103/PhysRevLett.121.021104

- Kritsuk, A. G., & Norman, M. L. 2004, ApJL, 601, L55, doi: 10.1086/381737
- McClure-Griffiths, N. M., Dickey, J. M., Gaensler, B. M., Green, A. J., & Haverkorn, M. 2006, ApJ, 652, 1339, doi: 10.1086/508706
- McKee, C. F., & Ostriker, J. P. 1977, ApJ, 218, 148, doi: 10.1086/155667
- Micelotta, E. R., Juvela, M., Padoan, P., et al. 2018, arXiv e-prints, arXiv:1810.10014.

https://arxiv.org/abs/1810.10014

- Ossenkopf-Okada, V., & Stepanov, R. 2019, A&A, 621, A5, doi: 10.1051/0004-6361/201731596
- Philcox, O. H. E., Sherwin, B. D., & van Engelen, A. e. 2018, MNRAS, 479, 5577, doi: 10.1093/mnras/sty1769
- Planck Collaboration, Adam, R., Ade, P. A. R., et al. 2016a, A&A, 586, A133,
 - $\mathbf{doi:}\ 10.1051/0004\text{-}6361/201425034$
- Planck Collaboration, Ade, P. A. R., Aghanim, N., et al. 2016b, A&A, 586, A141,

doi: 10.1051/0004-6361/201526506

Planck Collaboration, Akrami, Y., Ashdown, M., et al. 2018, ArXiv e-prints. https://arxiv.org/abs/1801.04945

- Redfield, S., & Linsky, J. L. 2004, ApJ, 613, 1004, doi: 10.1086/423311
- Remazeilles, M., Banday, A. J., Baccigalupi, C., et al. 2018, Journal of Cosmology and Astro-Particle Physics, 2018, 023, doi: 10.1088/1475-7516/2018/04/023
- Rotti, A., & Huffenberger, K. 2016, JCAP, 2016, 034, doi: 10.1088/1475-7516/2016/09/034
- —. 2019, JCAP, 2019, 045,doi: 10.1088/1475-7516/2019/01/045
- Schneider, M. D., & Bridle, S. 2010, MNRAS, 402, 2127, doi: 10.1111/j.1365-2966.2009.15956.x
- Seljak, U. 2000, MNRAS, 318, 203, doi: 10.1046/j.1365-8711.2000.03715.x
- Skalidis, R., & Pelgrims, V. 2019, A&A, 631, L11, doi: 10.1051/0004-6361/201936547
- Soler, J. D., Hennebelle, P., Martin, P. G., et al. 2013, ApJ, 774, 128, doi: 10.1088/0004-637X/774/2/128
- Thorne, B., Dunkley, J., Alonso, D., & Næss, S. 2017, MNRAS, 469, 2821, doi: 10.1093/mnras/stx949
- Vazquez-Semadeni, E. 2009, arXiv e-prints, arXiv:0902.0820. https://arxiv.org/abs/0902.0820
- Xu, S., Ji, S., & Lazarian, A. 2019, ApJ, 878, 157, doi: 10.3847/1538-4357/ab21be
- Yuen, K. H., Hu, Y., Lazarian, A., & Pogosyan, D. 2019, arXiv e-prints, arXiv:1904.03173. https://arxiv.org/abs/1904.03173
- Zaldarriaga, M. 2001, PhRvD, 64, 103001, doi: 10.1103/PhysRevD.64.103001

APPENDIX

A. DISTRIBUTIONS OF ANGLES

We describe the directions of (the long-axis of) the filament and the magnetic field with the coordinates in Fig. 3. The line of sight lies along the z-axis, while x-axis is down, and the y-axis is left. We assume that the filament (**L**) lies in the x-z plane, making angle θ_L to the line-of-sight. Equivalently, the directions can be expressed as a rotation around the y-axis:

$$\hat{\mathbf{L}} = \mathbf{R}_{\hat{\mathbf{v}}}(\theta_L)\hat{\mathbf{z}}.\tag{A1}$$

The magnetic field (**H**) we describe with respect to the filament axis, using spherical-polar coordinates (θ_{LH}, ϕ_{LH}):

$$\hat{\mathbf{H}} = \mathbf{R}_{\hat{\mathbf{L}}}(\phi_{LH})\mathbf{R}_{\hat{\mathbf{y}}}(\theta_{LH})\hat{\mathbf{L}} \tag{A2}$$

When we numerically generate realizations of these directions, we use the Rodrigues rotation formula to rotate the vectors around the proper axis. We use the distribution of θ_{LH} values to statistically characterize the misalignment in three dimensions between the filaments and their local magnetic fields.

An important quantity for computing the polarization of this filament is the angle that the magnetic field makes with the line-of-sight, expressed as:

$$\cos \theta_H = \hat{\mathbf{H}} \cdot \hat{\mathbf{z}}.\tag{A3}$$

When projected onto the plane of the sky, the filament and the field are separated by a misalignment angle ψ_{LH} , computed as:

$$\tan \psi_{LH} = \hat{H}_y / \hat{H}_x \tag{A4}$$

in the proper quadrant. For dust, the polarization angle relative to the filament direction is $\psi_{\rm pol} = \psi_{LH} + \pi/2$.

For a particular filament angle θ_L and field–filament misalignment θ_{LH} , changing the angle ϕ_{LH} rotates the field **H** to sweep out a cone around the filament direction. We can use the fact that $p(\phi_{LH})$ is uniform on $[0, 2\pi]$ to numerically accumulate the joint distribution of the field angle and projected field–filament misalignment:

$$p(\theta_H, \psi_{LH} | \theta_L, \theta_{LH}).$$
 (A5)

Because of the projections, this makes a loop of probability in the (θ_H, ψ_{LH}) parameter space. When the separation between the filament and field θ_{LH} is small, the loop centers tightly around $\theta_H = \theta_L$, $\psi_{LH} = 0$, and when θ_{LH} is larger, the loop is larger and more distorted.

If we make an assumption for the distribution of the field–filament misalignment angle θ_{LH} , we can marginalize over it.

$$p(\theta_H, \psi_{LH}|\theta_L) = \int d\theta_{LH} \, p(\theta_H, \psi_{LH}|\theta_L, \theta_{LH}) p(\theta_{LH}). \tag{A6}$$

In Fig. 8, we show this joint distribution for several filament directions, under the assumption that the misalignment angle is Gaussian distributed. For filaments along the line of sight (small θ_L), the distribution in projected angle (ψ_{LH}) is broad, which makes sense as variations in the angle ϕ_{LH} cause a wide variety of ψ_{LH} angles. In Fig. 9, we also examine the marginal distributions $p(\psi_{LH}|\theta_L)$ and $p(\theta_H|\theta_L)$. In Fig. 10, we further marginalize over the filament angles to get the distribution of the projected field–filament misalignment:

$$p(\psi_{LH}) = \int d\theta_L \, d\theta_H \, p(\psi_{LH} | \theta_L) p(\theta_L). \tag{A7}$$

These marginalized distribution have positive kurtosis and are more sharply peaked than the Gaussian distribution from which they are derived. It is important to note that the polarized flux in practice will depend both on the polarization fraction (dependent on $\sin^2 \theta_H$) and the optical depth (dependent on the filament physical size, aspect ratio, and orientation θ_L), and so the observed distribution of misalignment above some signal-to-noise cut will differ, and must be computed from the multidimensional distribution accounting for survey characteristics.

³ At the beginning we fixed the plane-of-sky orientation of the filament, but we could have favored the magnetic field instead, and by symmetry we should have $p(\theta_H|\theta_L) = p(\theta_L|\theta_H)$.

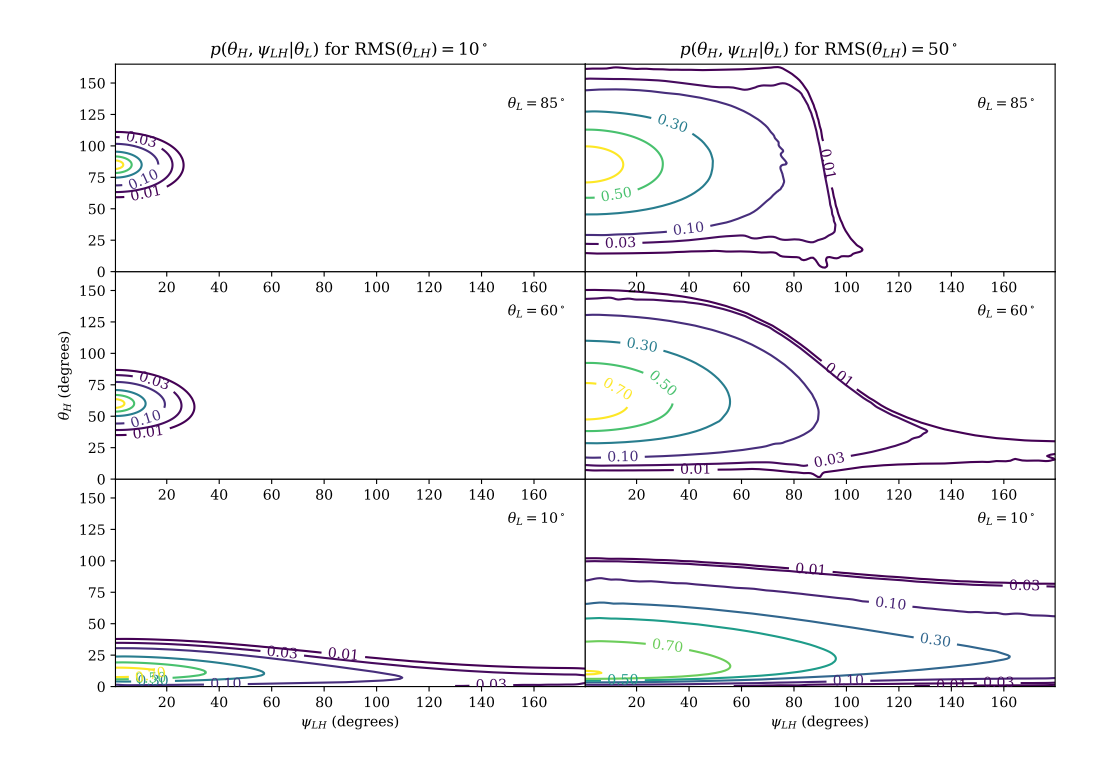


Figure 8. The joint distribution of the line-of-sight angle of the magnetic field (θ_H) and the projected angle between the magnetic field and the long-axis of the filament (ψ_{LH}) , under the assumption that the magnetic field direction has a Gaussian random distribution around the filament direction. The contours mark lines of constant probability density, and the number records the integrated probability outside the contour. The peak of the distribution is at $\psi_{LH} = 0^{\circ}$, $\theta_H = \theta_L$, corresponding to a filament aligned with the local magnetic field. The distribution is symmetric in the projected separation so we only show the half with $\psi_{LH} > 0^{\circ}$. In the left column, the field and filament are more closely aligned $(RMS(\theta_{LH}) = 10^{\circ})$ than in the right column $(RMS(\theta_{LH}) = 50^{\circ})$. In the top row, the filament is perpendicular to the line-of-sight $(\theta_L = 90^{\circ})$ and so is in the plane of the sky. In the bottom row, the filament aligns nearly along the line of sight $(\theta_L = 10^{\circ})$. For filaments along the line of sight (small θ_L), even a small misalignment with magnetic field can cause the projected angle (ψ_{LH}) to vary widely, and so the distribution of the projected angle is broad.

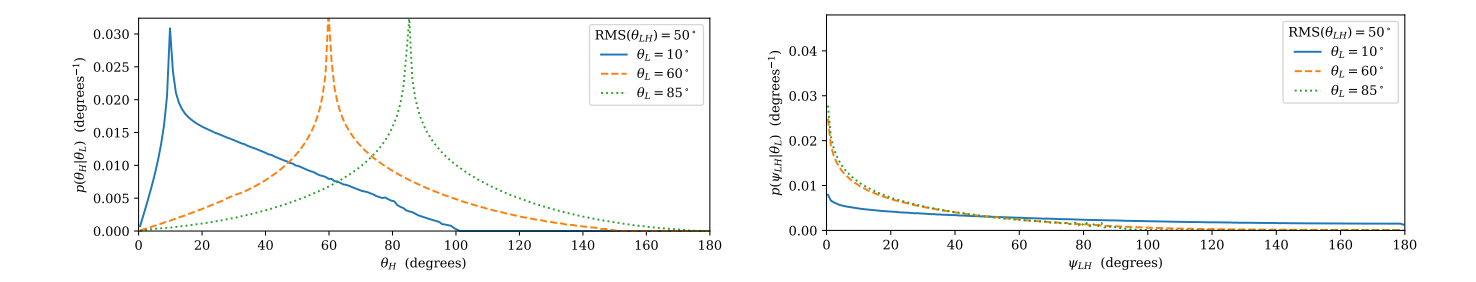


Figure 9. (Left) Distribution of the magnetic field angle, for three different filament angles, assuming a Gaussian distribution for the misalignment of the field and filament angle in three-dimensions. Each distribution peaks at the filament direction (for aligned filaments). (Right) Distribution of the projected misalignment between the filament and the magnetic field. The distribution is symmetric about $\psi_{LH} = 0^{\circ}$.

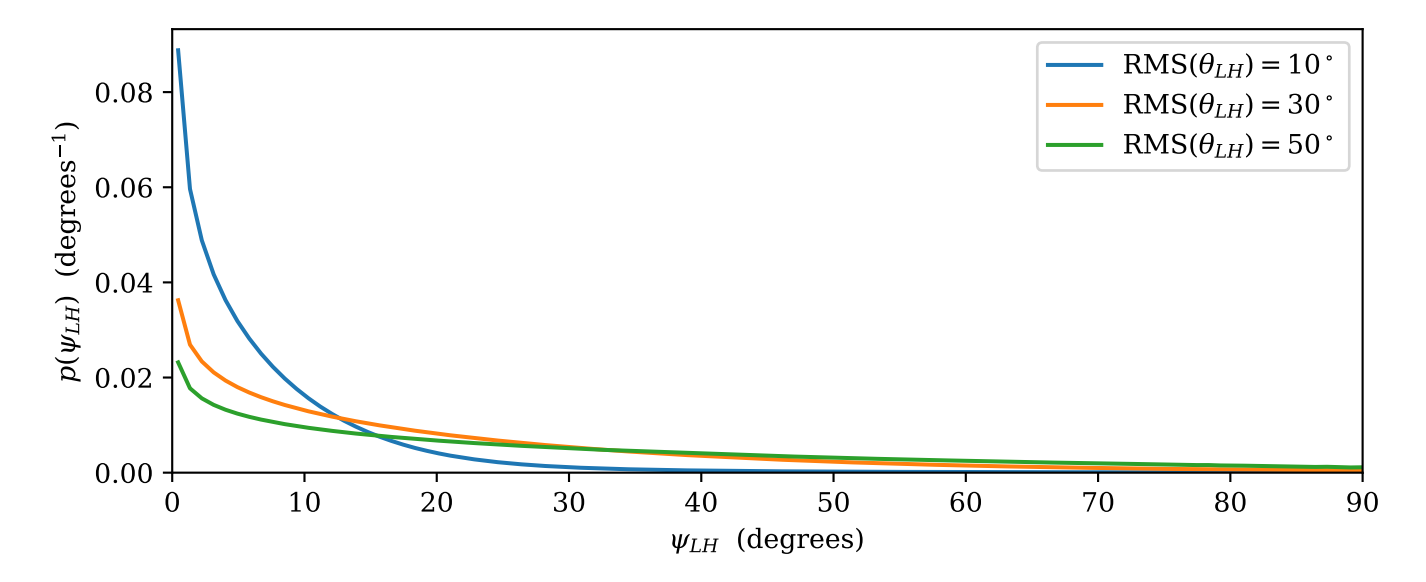


Figure 10. The distribution of the projected filament–field misalignment angle for randomly oriented filaments, under the assumption that the three-dimensional misalignment angle is Gaussian distributed, for various misalignment dispersions. The projected distribution is symmetric around $\psi_{LH}=0$.